CHEMISTRY OF MATERIALS

pubs.acs.org/cm
Article

Electronic and Lattice Distortions Induce Elastic Softening in Refractory Multicomponent Borides

Prince Sharma and Ganesh Balasubramanian*

Cite This: *Chem. Mater.* 2023, 35, 7511−7520
Read Online

ACCESS | Metrics & More | Article Recommendations | Supporting Information

ABSTRACT: Borides are extensively employed in applications demanding exceptionally high hardness, which arises from the unique and strong crystallographic arrangement of boron atoms therein. Addition of multiprincipal elements in borides is expected to enhance their structural properties due to lattice distortion and high configurational entropy. In contrast, we unravel a phenomenon of elastic softening in refractory multicomponent borides from first-principle predictions, which concur with experimentally determined metrics in their single-phase multiprincipal element counterparts. The reductions in the bulk and Young's modulus of these compounds are attributed to the lengthening and distortion of the boron−boron bonds and angles, but more critically to the perturbation in the charge densities arising from the different cations and the consequential increase in statistical weights of the d^5 configuration states of the transition metals present in the boride..

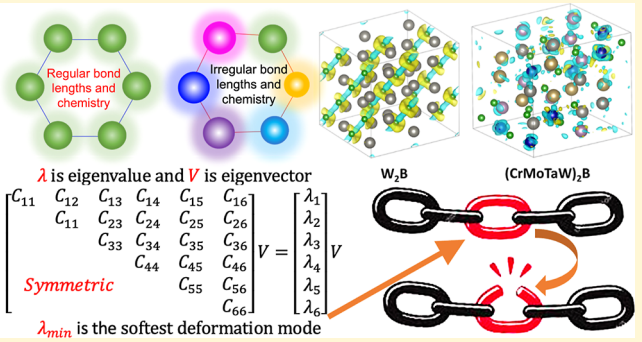

INTRODUCTION

Borides, an intriguing class of materials composed of boron and another element (typically a metal), are noted for their extraordinary high hardnesses.[1−3] A subset of this family, refractory metal borides, derives their elevated hardness from the crystallographic arrangement of the boron atoms and the strong covalent bonds between them. Predominantly, borides of refractory metals assume a hexagonal close-packed (HCP) lattice structure characterized by compactly organized layers of atoms held together by strong covalent bonds.[4−7] The boron atoms in a typical crystal are situated thus to form a strong three-dimensional network, while in metal borides, a cage-like atomic arrangement, *a.k.a.* a boron cluster, surrounded by metal atoms has been reported.[4−6,8−10] Such unique configurations enable borides to resist deformation under high pressures and temperatures, achieve a high melting point and enhanced stability at elevated temperatures, and be resistant to thermal shock under extreme conditions.[2,4,11,12] Given such remarkable material properties, borides are widely employed for cutting tools, wear-resistant coatings, and high-strength structural components, e.g., in aerospace.[4,12] When multiple different elements in near-equiatomic proportions occupy the nonboron sites instead of just a single species, the compound is termed as a multicomponent or "high-entropy" boride.[13−15] The latter term has its genesis from high-entropy alloys, so-called because of the enhanced material stability that is attributed to their high configurational entropy of mixing.[16,17]

The extent of hardening in metal borides depends on two key parameters, *viz.*, intrinsic and extrinsic hardening factors.[18] While intrinsic hardening is influenced by the metal-to-boron ratio and the arrangement of boron atoms, extrinsic effects emerge at the microstructural scale and involve the grain size, number of crystallographic phases, as well as segregations present in the material. Multicomponent borides generally do not form a single phase (see Supporting Information) and are contaminated with impurities like oxides and B_4C,[19−27] promoting segregation at the grain boundaries and hence an increased hardness due to the foregoing extrinsic effects. In contrast, and notably so, we find that single-phase multicomponent borides have lower hardness than their precursor counterparts.[14,28−31] Here, we examine the fundamental mechanisms associated with the intrinsic factors for hardness reduction in multicomponent borides. While the literature extensively reports on diborides, we expand our analyses to monoborides and dimetal borides as well. Employing first-principles calculations, we compute the hardnesses of two single-phase diborides reported in the literature and compare our predictions against those of the precursor materials. Our

Received: May 9, 2023
Revised: August 31, 2023
Published: September 15, 2023

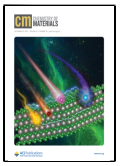

https://doi.org/10.1021/acs.chemmater.3c01086
Chem. Mater. 2023, 35, 7511−7520

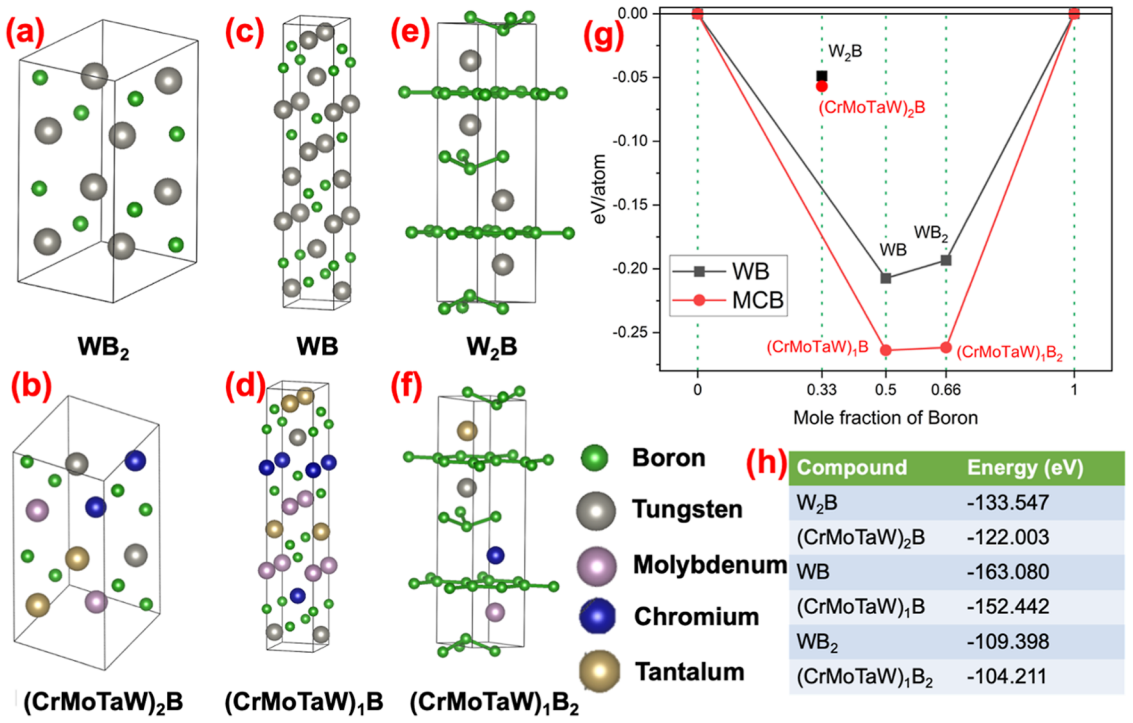

(h)

Compound	Energy (eV)
W_2B	-133.547
$(CrMoTaW)_2B$	-122.003
WB	-163.080
$(CrMoTaW)_1B$	-152.442
WB_2	-109.398
$(CrMoTaW)_1B_2$	-104.211

Figure 1. Crystal structures of (a) W_2B; (b) $(CrMoTaW)_2B$; (c) WB; (d) $(CrMoTaW)_1B$; (e) WB_2; (f) $(CrMoTaW)_1B_2$ are illustrated with green, gray, golden, blue, and purple atoms representing boron, tungsten, tantalum, chromium, and molybdenum, respectively. (g) Thermodynamic convex hull of W−B and the multicomponent (CrMoTaW)−B (denoted as MCB) system are reproduced from the formation energies per atom for the structures shown in (a−f). (h) Total formation energies of fully relaxed borides in (a−f) are listed.

results, elaborated below, reveal for the first time that distortion of boron−boron (B−B) bonds and perturbation in charge densities due to metal atoms are the root causes for such hardness decrement.

RESULTS

The crystal structures and the corresponding formation energies per atom for tungsten (W) and multicomponent borides are displayed in Figure 1a−f. The total formation energies in Figure 1h indicate that multicomponent borides/diborides are higher relative to their corresponding W counterparts with an equal mole fraction of boron; we attribute this result to the formation energies of Cr (−11.93 eV), Mo (−10.33 eV), and Ta (−11.73 eV) being higher than those of W (−13.27 eV). Nonetheless, the formation enthalpy $\Delta E = E(A_xB_yC_z) - xE(A) - yE(B) - zE(C)$ derived from the differences of elemental energies from that of the compound proves that the multicomponent borides are thermodynamically more stable compared to W-borides. This prediction is corroborated by the convex hull diagram presented in Figure 1g. The enthalpies for WB and WB_2 are −0.207 and −0.193 eV/atom, while for $(CrMoTaW)_1B$ and $(CrMoTaW)_1B_2$, they are −0.270 and −0.262 eV/atom, respectively. We note that monoborides are energetically most favorable, and a similar trend is reported in the literature,[32−34] while thermodynamically, the formation energy of multicomponent diborides is nearly equal to that of the multicomponent monoboride. As the mole fraction of boron increases, the distance between W atoms increases and the B−B bond length decreases. For optimal (high) stability, all pairwise bonds among the elements of a compound must be strong; this condition is met only when both W−W and B−B bonds are of intermediate length, and hence monoborides are rendered usually more stable relative to other stoichiometric borides. We note that the increase in energy due to the chaotic charge distributions among cations and boron atoms in multicomponent monoborides is not significant. Hence, their enthalpy of formation is similar to that of multicomponent diboride that has a distorted but strong B−B bond. The predictions also indicate that $(CrMoTaW)_2B$ and W_2B are the least stable compounds among the examined materials.

Figure 2 illustrates the variation of bulk modulus, shear modulus, Young's modulus, and hardness as a function of the mole fraction of B. In general, the magnitudes of all the structural properties increase with increasing concentrations of B in both W and multicomponent borides. Since bulk modulus is directly related to the bond strength of elements, a notable drop is recorded only for the bulk modulus when the chemistry changes from WB to WB_2, possibly due to variations in bond strength. Nonetheless, the corresponding predictions are similar for the multicomponent borides (MCBs), *i.e.*, 273.06 GPa for $(CrMoTaW)_1B$ and 272.87 GPa for $(CrMoTaW)_1B_2$. This negligible change in the bulk moduli of the MCBs is attributed to the nonuniformity in the charge concentrations caused by different cationic species, which enhances the interactions between the boron layers and the metal cations.

Shear modulus, Young's modulus, and hardness of multicomponent borides increase with increasing fraction of B in the compound but are consistently lower than their W counterparts (∼2−3 GPa for shear modulus and hardness, ∼20−30 GPa for Young's modulus). Nonetheless, the trends in the variation of these structural properties suggest a degree of elastic softening of the multicomponent borides. For instance, the increase in bulk modulus for both types of borides is significantly large, ranging from ∼50−80 GPa. The extensive differences arise from the inclusion of various cationic species

https://doi.org/10.1021/acs.chemmater.3c01086
Chem. Mater. 2023, 35, 7511−7520

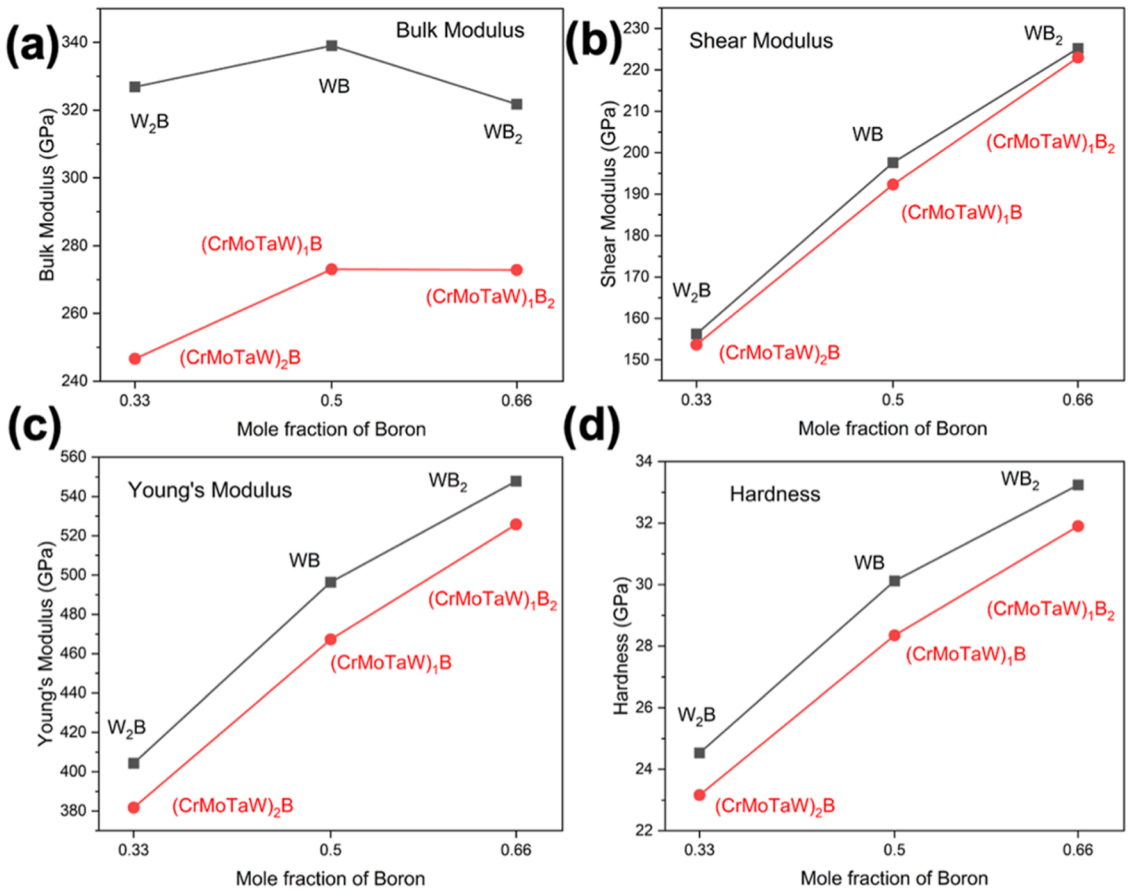

Figure 2. Structural properties (in GPa) for W and multicomponent borides with variations in B mole fraction are presented: (a) bulk modulus; (b) shear modulus; (c) Young's modulus; and (d) hardness. The plots reveal an enhancement in the structural properties with an increase in B concentration, while the properties of the multicomponent borides are consistently reduced from the W counterparts.

Table 1. Simulated Borides and the Corresponding Elastic Tensor Constants (C_{11}, C_{12}, C_{44}, and C_{66}), Minimum Eigenvalue (λ_{min}) of the Elastic Tensor Matrix, and Elastic Moduli Are Listed

compound	C_{11} (GPa)	C_{12} (GPa)	C_{44} (GPa)	C_{66} (GPa)	λ_{min} (GPa)	bulk modulus (GPa)	Shear modulus (GPa)	Young's modulus (GPa)
$(CrMoTaW)_2B$	446.92	140.62	161.79	137.93	135.02	246.63	153.66	381.71
W_2B	546.02	205.32	147.12	171.99	147.12	326.87	156.25	404.31
$(CrMoTaW)_1B$	493.67	164.79	200.32	238.75	197.97	273.06	192.31	467.24
WB	553.50	231.85	219.15	246.16	219.20	339.05	197.63	496.41
$(CrMoTaW)_1B_2$	558.72	125.74	222.13	220.74	217.28	272.87	223.01	525.79
WB_2	598.20	145.39	224.90	226.90	224.91	321.78	225.18	547.77

in the supercell, perturbing the charge distribution in the lattice structure and making it soft and susceptible to compression. The dissimilarities in the atomic radii of the cations cause the bond lengths to be irregular and the bond angles to be distorted. Also, variations in the principal quantum number and valence electron configuration in the d-shell of the cations disrupt the bond characteristics and initiate a polarity. During a shear deformation, the in-plane layer of B atoms maintains the lattice structure intact; however, the disparity between W and multicomponent borides is driven by the distortion in the bond angles and lengths produced by the different cations.

Table 1 lists the elastic tensors C_{11}, C_{12}, C_{44}, and C_{66} together with the minimum eigenvalue (λ_{min}) in the elastic tensor, Young's, shear, and bulk moduli. The variations in the elastic tensor constants underline the root causes that contribute to changes in the elastic moduli. We note that the tensor constants for W and multicomponent borides vary between 100 and 40 GPa for C_{11}, to 60−25 GPa for C_{12}, and ∼20 GPa for C_{44}. Such differences indicate that softening due to planar loading is more pronounced relative to shear loading. Shear strength is governed by the attractive forces between the interatomic layers of B and the metal cations. Thus, one can infer that the interatomic distances between B atoms in successive layers of a multicomponent boride are less impacted than those bonds colocated on a plane. Since elastic constants are determined in the elastic regime and hardness is measured from plastic deformation, it is nontrivial to correlate elastic tensor and hardness. The eigenvalues of an elastic tensor are independent of each other and are reflective of the material's ability to resist deformation under independent elastic modes.[35] Hence, hardness is governed by the softest elastic mode irrespective of the magnitude of the elastic constants—a typical bucket effect where a chain is as strong as its weakest link. Here we note that the ratio of hardness presented in

https://doi.org/10.1021/acs.chemmater.3c01086
Chem. Mater. 2023, 35, 7511−7520

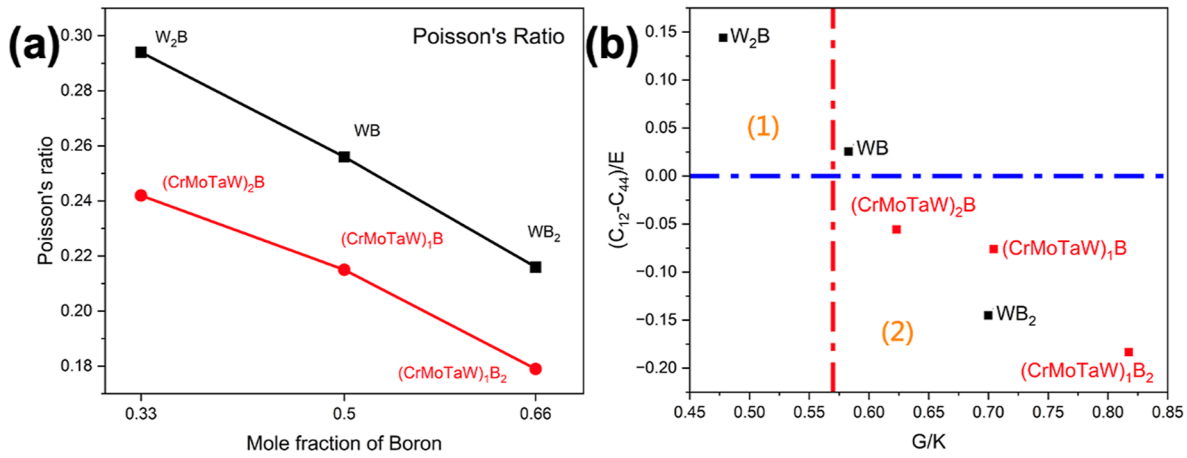

Figure 3. (a) Poisson's ratio of multicomponent and *W* borides as a function of the mole fraction of boron. (b) Correlation between the Pugh ratio (G/K) and Cauchy's pressure normalized by Young's modulus (E) for the borides distributed across the ductile (1) and brittle (2) regions. The discontinuous vertical (red) line corresponds to $G/B = 0.57$, and the horizontal (blue) discontinuous line highlights the Pettifor criterion where $C_{12}-C_{44} = 0$.

Figure 2d and corresponding λ_{min} in Table 1 lies between 0.13 and 0.17.

Poisson's ratio decreases linearly with an increase in B mole fraction, and that for multicomponent borides is consistently lower than that for their W counterparts (Figure 3a). This result substantiates the importance of probing the elastic tensor and the elastic constants. Poisson's ratio is the quotient of transverse strain due to axial load to the axial strain on a crystal and can be computed from a ratio of the difference of multiples of K (bulk modulus) and G (shear modulus) to the sum of multiples of K and G. From Table 1 and Figure 2, we note that the reductions in G for multicomponent borides (compared to *W* borides) are trivial relative to corresponding reductions in K, and hence the Poisson's ratio for multicomponent borides is lower than their *W* counterparts. Physically, if one is to load both types of corresponding borides by an identical axial weight (within the elastic limit), the axial strain in multicomponent borides will be lower (C_{11} and K are smaller) compared to *W*-borides; on the other hand, the transverse strain due to the axial load will be limited owing to the relatively less variations in C_{44} and G. Thus, axial yielding in multicomponent borides is more extended under similar loading conditions as compared to *W* borides, while variations in transverse yields are insignificant, decreasing the Poisson's ratio for multicomponent borides. This finding suggests that the low Poisson's ratio of multicomponent borides renders them desirable for applications that necessitate restricted shape variation in the transverse direction in response to tensile or compressive stress along the longitudinal direction.

Figure 3b exhibits Young's modulus normalized Cauchy pressure as a function of the Pugh ratio (G/K), with region (1) indicative of a ductile material with predominantly metallic bonding and region (2) representative of brittle materials dominated by covalent bonding. A low Pugh ratio and high Cauchy pressure corroborate a ductile behavior, albeit with notable exceptions, *e.g.*, materials such as $NbCr_2$ with Laves phases. Crucially, these metrics do not consider the effects of crystal structure or anisotropy and offer a general guideline for assessing material ductility. Nevertheless, borides being extremely brittle, the distortion in bond lengths and angles reduces K more than G due to the "caging" effect of boron layers, and hence the Pugh's ratio assumes a relatively higher value for multicomponent borides.

Upon a deeper evaluation of the relaxed boride supercells, we find significant elongation and distortion in B−B bond lengths and angles for multicomponent borides (Table 2). The

Table 2. Variations in Boron−Boron Bond Lengths and Bond Angle Distortions for *W* and Multicomponent Borides

compound	bond length (Å)	bond angle (deg)	
$(CrMoTaW)_2B$	2.62−2.91	177.44−182.56	
W_2B	2.398	180	
$(CrMoTaW)_1B$	1.85	114.04−118.14	
WB	1.81	120.195	
$(CrMoTaW)_1B_2$	1.838−1.841	113.778	buckled boron layer
	1.728−1.741	distortion by 1°	planar boron layer
WB_2	1.824	111.69	buckled boron layer
	1.743	120	planar boron layer

degree of distortion increases with increase in mole fraction of metal cations. The percentage elongation in bond length for $(CrMoTaW)_2B$ ranges between 9.25 and 21.35%; for $(CrMoTaW)_1B$, it is 2.21%; and for $(CrMoTaW)_1B_2$, the variation is 0.77−0.93%. The distortion in the bond angles follows a similar trend, being approximately 2.5, 2−4, and 1° for $(CrMoTaW)_2B$, $(CrMoTaW)_1B$, and $(CrMoTaW)_1B_2$, respectively.

The bond angle distortion in a compound impacts its hardness. In general, a compound with a higher symmetry and an ordered arrangement of atoms will be harder than one with distortions because a symmetrical atomic configuration results in stronger chemical bonds, making deformation more difficult.[1,36−38] When bond angles are distorted, the disorder in the crystal structure promotes relatively weaker chemical bonds and a softer material. When the degree of bond angle distortion increases, an enhanced disorder renders the material susceptible to deformations. Additionally, an increased bond angle distortion contributes to increased defects that further weaken the chemical bonds and soften the compound. Likewise, while shorter bond lengths enable stronger chemical

https://doi.org/10.1021/acs.chemmater.3c01086
Chem. Mater. 2023, 35, 7511−7520

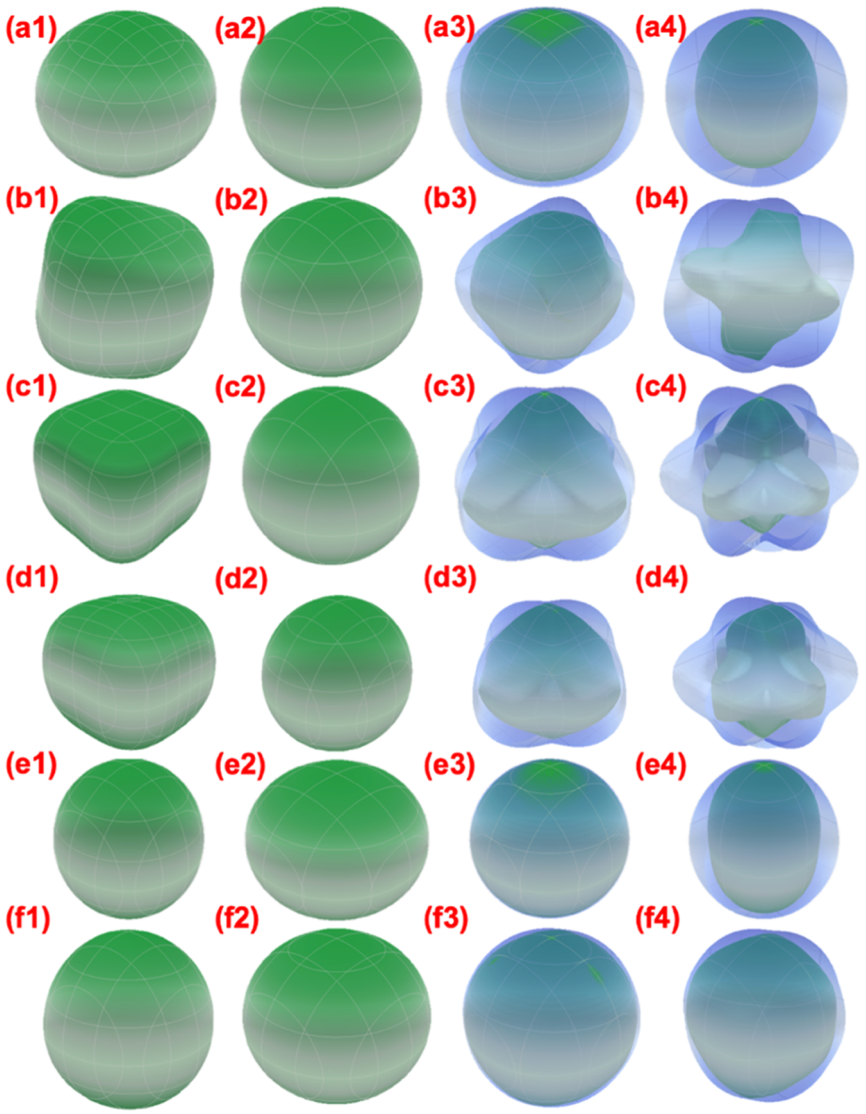

Figure 4. 3D visualizations of Young's modulus (GPa), linear compressibility (TPa^{-1}), shear modulus (GPa), and Poisson's ratio for tungsten and multicomponent borides. (a1, b1, c1, d1, e1, and f1) reproduce Young's modulus for W_2B, $(CrMoTaW)_2B$, WB, $(CrMoTaW)_1B$, WB_2, and $(CrMoTaW)_1B_2$, respectively; (a2, b2, c2, d2, e2, and f2) are 3D visuals of linear compressibility for W_2B, $(CrMoTaW)_2B$, WB, $(CrMoTaW)_1B$, WB_2, and $(CrMoTaW)_1B_2$, respectively; (a3, b3, c3, d3, e3, and f3) depict 3D visualization of shear modulus for W_2B, $(CrMoTaW)_2B$, WB, $(CrMoTaW)_1B$, WB_2 and $(CrMoTaW)_1B_2$, respectively; (a4, b4, c4, d4, and f4) present pictorial versions of Poisson's ratio for W_2B, $(CrMoTaW)_2B$, WB, $(CrMoTaW)_1B$, WB_2, and $(CrMoTaW)_1B_2$, respectively.

bonds, impeding deformation and hardening the material,[38,39] below a threshold, extremely short bonds cause the compound to be prone to brittle failure. Variations in bond lengths direct to lattice distortions that is typically considered to enhance structural properties in high-entropy and multiprincipal element materials.[40−42] In contrast, here we find that distortion in the lattice structure of the borides is potentially detrimental to their mechanical properties and contributes to softening.

Next, we examine elastic anisotropy through a 3D pictorial representation of the elastic properties of the borides (Figure 4). For an isotropic material, the visualization renders a spherical shape denoting a limited dependence on the direction of loading, while distorted spheres are characteristic of anisotropy. The blue and green curves reflect the maximum and minimum estimates of the shear modulus and Poisson's ratio, respectively. Among dimetal borides, multicomponent materials display higher anisotropy, while W_2B is near-ideal isotropic with slight deviations. The cuboidal 3D representation for Young's modulus of $(CrMoTaW)_2B$ suggests symmetric effects with a high degree of anisotropy, while the linear compressibility for both W and multicomponent borides is isotropic. W_2B assumes low anisotropy in shear modulus and Poisson's ratio, unlike $(CrMoTaW)_2B$, which is strongly anisotropic. We correlate the variations in Young's modulus, shear modulus, and Poisson's ratio of $(CrMoTaW)_2B$ to the distorted bond angles, nonuniformity of bond lengths, and the cumulative effect of electronic environments generated by Cr, Mo, Ta, and W atoms. The presence of multiple principal elements distorts the symmetry and produces several nonzero elements in the elastic tensor, which in turn enhances the anisotropy. $(CrMoTaW)_1B$ and WB follow similar directional characteristics for their structural properties. The maximum and minimum surfaces for the shear modulus and Poisson's ratio are predominantly anisotropic, as noted from a completely distorted surface. Now, diborides have isotropic Young's modulus with a higher value along the z direction and

https://doi.org/10.1021/acs.chemmater.3c01086
Chem. Mater. 2023, 35, 7511−7520

linear compressibility like the above-discussed borides with higher values in the *xy* plane. The Poisson's ratio of WB_2 is higher in the *z* direction, although $(CrMoTaW)_1B_2$ has a distorted surface. Young's modulus assumes a higher magnitude in the *z* direction due to the presence of boron layers in the *xy* plane; these layers also contribute to increases in the linear compressibility along that plane and reduce it along the orthogonal *z* direction. The effect of buckled boron layers is noted from the distortion in Poisson's ratio, whereas variation in bond lengths and angles will induce the strains to be nonuniform along the perpendicular directions.

Most multicomponent borides have heterogeneities consisting of B_4C, graphite, $(Zr/Hf)O_2$, and segregates of unitary or mixed-phase borides.[19−27] These heterogeneities emerge at grain boundaries and improve the structural properties relative to those of their single-phase counterparts. These impurities get impregnated during material synthesis, typically *via* mechanical alloying and sintering of metal oxides in the presence of B_4C. Monitoring and precise control of the proportion of such impurities is challenging; hence, estimating the hardness of a pure single-phase material devoid of grain boundary segregations is difficult and requires optimal synthesis methods that minimize exposure to oxide and carbonaceous contents.[14,24,28−31,43] A widely reported multicomponent boride $(Hf_{0.2}Zr_{0.2}Ta_{0.2}Nb_{0.2}Ti_{0.2})B_2$ has been reported to possess hardness between 16.4 and 25.4 GPa from experimental measurements,[14,21,22,24,29,31,44−46] with its single phase chemistry assuming 16.4[46] and 20.9 GPa[43] per the literature. Similarly, the hardness of another multicomponent boride $(Hf_{0.2}Zr_{0.2}Ti_{0.2}Ta_{0.2}Cr_{0.2})B_2$ is recorded to range from 19.9 to 29.3 GPa, while its single-phase structures have a hardness between 19.9 and 25.4 GPa.[14,26,27,31] A case in point is that single-phase multicomponent borides have a lower hardness relative to their precursor metal diborides.

From first-principle predictions in the literature, we note that the mechanical properties for $(Hf_{0.2}Zr_{0.2}Ta_{0.2}M_{0.2}Ti_{0.2})B_2$, where M = {Nb, Mo, and Cr}, are typically reduced or nearly equal to those of the constituent metal diborides; this difference is more pronounced for the bulk modulus as only ZrB_2 and TiB_2 assume slightly lower values relative to the MCBs.[47] In the case of shear moduli, only MoB_2 and CrB_2 have lower magnitudes as compared to the MCB with the lowest shear modulus. Also, Qiao *et al.* validate our hypothesis by virtual crystal approximation method.[48] Structural properties of $(TiZrHfNbTa)B_2$, $(TiZrHfNbMo)B_2$, $(TiZrHfTaMo)B_2$, $(TiZrNbTaMo)B_2$, and $(TiHfNbTaMo)B_2$ multicomponent borides have been compared with those of single principal component borides.[49] The results have suggested that the bulk modulus of all the multicomponent borides is inferior to that of NbB_2, TaB_2, and MoB_2. Kavak *et al.* predict the hardness of $(HfTiWZr)_1B_2$ from first-principle calculations to be 30.99 GPa,[19] which is less than the theoretical/experimental (36/35.5 GPa) hardness value of TiB_2.[50,51] In the same vein, molecular dynamics simulations of $(Ti_{0.2}Zr_{0.2}Hf_{0.2}Nb_{0.2}Ta_{0.2})B_2$ using deep learning potentials[52] have resulted in values akin to the experiments and density functional theory (DFT) calculations. In a recent study, we find multicomponent silicides to exhibit a similar trend of reduction in bulk modulus from unitary to quinary disilicides.[53] Overall, the indicators in the literature strongly corroborate and robustify our hypothesis about the phenomenon of elastic softening in multicomponent borides. We perform DFT computations for two multicomponent boride compositions reported in the literature to substantiate our premise. For $(Mo_{0.2}Zr_{0.2}Ta_{0.2}Nb_{0.2}Ti_{0.2})B_2$,[14] the theoretical hardness is 37.41 GPa, while we predict the hardness of TiB_2 from our calculations to be 40.24 GPa. Similarly, for $(TiVZrHf)_1Br_2$,[30] the DFT prediction for hardness is 36.98 GPa, which is lower than that for TiB_2.

We select cations with similar electronic states to ensure a minimal change in the chemistry of the compound. Increase in the number of d^5 states destabilizes the sp^2 hybridization in planar boron layers due to the localization of electrons and hence is detrimental to the predicted structural properties.[1] Although the cations Cr, Mo, and W have a similar outer shell electronic configuration with an increasing number of principal quantum states, we note a significant distortion in the distributions of the charge densities, elucidated from the juxtaposing charge densities obtained from Bader charge analysis (Figure 5). In Figure 5a,b, the charge density around

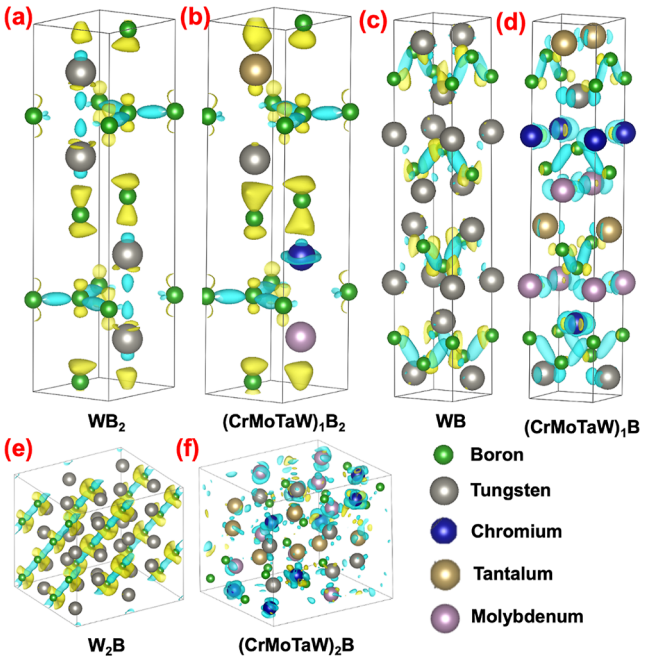

Figure 5. Bader charge analysis of W and multicomponent borides. (a) WB_2 supercell displaying a uniform charge distribution around the B−B layer and metal atoms; (b) $(CrMoTaW)_1B_2$ shows a significant amount of charge localized around metal atoms; (c) WB exhibits similar behavior as WB_2; (d) $(CrMoTaW)_1B$ produces an increment in charge densities around metal cations; (e) W_2B has uniform bonds with similar charge densities; (f) $(CrMoTaW)_2B$ reproduces non uniformity and chaos in the charge distribution and density.

the metal cations in WB_2 is uniformly distributed, while for $(CrMoTaW)_1B_2$, it is nonuniform, *i.e.*, the charges are concentrated around chromium; also, the charge that is localized at the center of the planar boron layer in WB_2 is delocalized in the case of $(CrMoTaW)_1B_2$. This result implies a significant rise in the statistical weight of d^5 states in transition metals and a distortion in the sp^2 geometry of the planar boron layer. In the case of monoborides, presented in Figure 5c,d, we observe a similar behavior; in contrast to the charge that is localized around B−B bonds in WB, in $(CrMoTaW)_1B$ there is an increase in charge densities around the transition metal atoms. In monoborides, the statistical weight of d^5 configuration states is even greater relative to $(CrMoTaW)_1B_2$. In Figure 5e,f, the difference is even more

https://doi.org/10.1021/acs.chemmater.3c01086
Chem. Mater. 2023, 35, 7511−7520

explicit as we characterize ordered and symmetrical bonding in W_2B and a rather electronic chaos in $(CrMoTaW)_2B$. Notably, this electronic disruption is the primary reason for the largest reduction of the bulk modulus. Here, the statistical weight of d^5 configuration states for the transition metal atoms increases drastically, which delocalizes electrons from the B−B bonds, thereby weakening them. Closing the loop, we can now correlate this observation with the lengthening and angular distortions of B−B bonds reported above in Table 2. The increase in bond lengths is attributed to the weakening and delocalization of charges from the B−B bonds.

The trend in the variation of the structural properties concurs with the differences in the charge distribution on W and multicomponent borides. As the stoichiometric coefficient of boron increases and the electrons are transferred to the boron sublattice, the primary function in the electronic structure of the compound is now performed by the sp states of boron and B−B bonds. So, with an increase in the boron mole fraction in the boride, the B−B bonds become shorter and require additional electron donor atoms in the compound. Given that B−B bond behavior controls the response to external stimulus, their formation through sp^2 hybridization results in a stable and saturated electronic structure like that found in graphitic layers. Thus, sp^2 hybridization serves as the backbone of transition-metal borides. The B−B bond is a strongly directional covalent bond and is resistant to deformation/dissociation even under extreme loads. However, the softer elastic properties of multicomponent borides are related to disruption of the lengthened B−B bonds under stress. The weakness of the covalent bond is due to a limited transfer of electrons to the boron layer, reducing the directionality of the B−B bonds. The electrons are not completely centered between the two boron atoms but rather deviate from the boron layer. This type of sp^2 hybridization results in a distorted electron center as the hybrid orbital forms at an angle rather than a straight line. The distortion of the sp^2 hybridization in B−B bonds in multicomponent borides is ascribed to the boron atom having only three valence electrons that is insufficient to create strong sp^2 covalent bonds between boron atoms as well as for metal−boron bonds.[1,54,55] Additionally, in the case of multicomponent borides, the transition metal atoms withhold even more electrons compared to when only W is present in the lattice. A limitation of electrons not only decreases the strength of the bonds but also impedes the mechanics of the material. Hence, the weakening of the B−B bonds is caused by a deficiency of electron transfer.

DISCUSSION

We employ first-principles calculations to probe the phenomenon of elastic softening in refractory multicomponent *a.k.a.* "high entropy" borides. Our predictions reveal that the mole fraction of boron imparts a strong contribution in enhancing the structural properties of multiprincipal element borides. Although the (CrMoTaW)-based refractory borides considered herein have a higher total energy, the lower formation energies of individual dopants render them thermodynamically more stable relative to the W borides. Our results assert that lattice distortion in multicomponent borides perturbs B−B bonds, contributes to elastic softening, and suppresses structural properties. On the other hand, shear modulus is relatively less impacted because it depends on a plane of shear that is usually aligned with the boron layers in the lattice. The hardness is directly governed by λ_{min} corresponding to the softest elastic mode. However, due to the lengthening of the bonds and angular distortions, the boride becomes more compressible, resulting in a higher reduction in bulk and Young's moduli. All refractory multicomponent boride samples examined here assume reduced elastic modulus, elastic tensor eigenvalues, and hardness compared to their W counterparts. The elastic properties and hardness of single-phase multicomponent borides reported in the literature are validated through our calculations, which corroborate the elastic softening due to an increase in B−B bond length that weakens the covalent bond strength.

Most remarkably, single-phase refractory multicomponent borides do not experience ultrahigh hardness relative to their unitary counterparts, contrary to the literature on high-entropy alloys that suggest lattice distortion, configurational entropy, and the cocktail effect promote elevated structural properties. In comparison to the "high" entropy of atomic configuration, the statistical weights of electronic configurational states are vital to the stability and structural properties of refractory multiprincipal elements in borides. A scrutiny of the bond chemistry of anions in borides can enable a designer selection of cations to produce multicomponent borides with targeted properties.

METHODS

Density Functional Theory. Vienna ab initio Simulation Package (VASP) together with the Vaspkit is used to perform the DFT calculations.[56,57] The ATAT[58] enabled MCSQS technique is adopted to create the (random) supercells of the multicomponent borides. Electronic configurations [He] $2s^2$ $2p^1$, [Ar] $3d^5$ $4s^1$, [Kr] $4d^5$ $5s^1$, [Kr] $4d^5$ $5s^1$, [Xe] $4f^{14}$ $5d^3$ $6s^2$, and [Xe] $6s^1$ $4f^{14}$ $5d^5$ are used to represent B, Cr, Ta, Mo, Ta, and W, respectively. Projector-augmented wave function (PAW) pseudopotentials are used to describe the core electrons.[59] Using 0.1 eV for the gamma parameter, the Perdew−Burke−Ernzerhof (PBE) parametrized generalized gradient approximation (GGA) exchange correlation functional is employed with the Methfessel−Paxton smearing scheme.[60,61] An energy cutoff of 400 eV is considered for the planewave expansion. For integration of the Brillouin zone, a *K*-point mesh with an accuracy level of 0.02 is generated using the Monkhorst−Pack method.[62] A convergence criterion between two iterations is set at 10^{-8} eV to resolve the Kohn−Sham equations by a self-consistent field procedure. Several relaxation steps (with ISIF = 2 and 7, alternatively) are performed to fully relax the supercell volume and the atom positions, separately.

The second-order elastic tensors (SOET) are computed using the finite difference method on the Hessian of the total energy with respect to the positions of the atoms. Within the linear elastic zone, Hooke's law assumes the form $\sigma_{ij} = C_{ijkl}\varepsilon_{kl}$. Here, σ_{ij} and ε_{kl} define the stress and strain second rank tensors, and hence, C_{ijkl} is the fourth rank elastic stiffness tensor. Note that $C_{ijkl} = \frac{\partial^2 U}{\partial\varepsilon_{ij}\partial\varepsilon_{kl}}$, where U is the strain energy calculated from DFT. Initially, there are 81 tensors for C_{ijkl}, but with the symmetry of stress and strain tensors, they are reduced to 21 tensors.[63] To represent the stress and strain tensors as six-dimensional vectors, we use the following simplified Voigt notations

$$[\sigma_{xx}\sigma_{yy}\sigma_{zz}\sigma_{yz}\sigma_{xz}\sigma_{xy}] = [\sigma_1\sigma_2\sigma_3\sigma_4\sigma_5\sigma_6],$$
$$[\varepsilon_{xx}\varepsilon_{yy}\varepsilon_{zz}\varepsilon_{yz}\varepsilon_{xz}\varepsilon_{xy}] = [\varepsilon_1\varepsilon_2\varepsilon_3\varepsilon_4\varepsilon_5\varepsilon_6]$$

For a simplified representation of the elastic stiffness tensor, we use Voigt notations accordingly:

Eleven ≡ 1; 22 ≡ 2; 33 ≡ 3; 23(32) ≡ 4; 13(31) ≡ 5; 12(21) ≡ 6. Thus

https://doi.org/10.1021/acs.chemmater.3c01086
Chem. Mater. 2023, 35, 7511−7520

$$\begin{bmatrix}\sigma_1\\ \sigma_2\\ \sigma_3\\ \sigma_4\\ \sigma_5\\ \sigma_6\end{bmatrix} = \begin{bmatrix} C_{11} & C_{12} & C_{13} & C_{14} & C_{15} & C_{16}\\ & C_{22} & C_{23} & C_{24} & C_{25} & C_{26}\\ & & C_{33} & C_{34} & C_{35} & C_{36}\\ & & & C_{44} & C_{45} & C_{46}\\ & & & & C_{55} & C_{56}\\ & & & & & C_{66}\end{bmatrix}\begin{bmatrix}\varepsilon_1\\ \varepsilon_2\\ \varepsilon_3\\ \varepsilon_4\\ \varepsilon_5\\ \varepsilon_6\end{bmatrix}$$

Symmetric

The analytical approach described above is applicable to the least symmetric crystal system of a triclinic structure. However, with increasing symmetry in monoclinic, orthorhombic, tetragonal, hexagonal, and cubic lattices, the 21 independent elastic tensors reduce to 13, 9, 7, 5, and 3, respectively.[63] The inverse of the elastic tensor matrix produces an elastic compliance matrix, $s_{ij} = C_{ij}^{-1}$. To calculate the polycrystalline bulk and shear modulus, we use Voigt (represented by subscript V) and Reuss (represented by subscript R) averaging schemes.

bulk modulus (Voigt),

$$K_V = \frac{[(C_{11} + C_{22} + C_{33}) + 2(C_{12} + C_{23} + C_{31})]}{9}$$

shear modulus (Voigt),

$$G_V = \frac{[(C_{11} + C_{22} + C_{33}) - (C_{12} + C_{23} + C_{31}) + 3(C_{44} + C_{55} + C_{66})]}{15}$$

bulk modulus (Reuss),

$$K_R = \frac{1}{[(s_{11} + s_{22} + s_{33}) + 2(s_{12} + s_{23} + s_{31})]}$$

shear modulus (Reuss),

$$G_R = \frac{15}{[4(s_{11} + s_{22} + s_{33}) - 4(s_{12} + s_{23} + s_{31}) + 3(s_{44} + s_{55} + s_{66})]}$$

The predicted bulk and shear moduli $K = \frac{K_V + K_R}{2}$ and $G = \frac{G_V + G_R}{2}$. Additionally, Young's modulus (E), Poison's ratio (ϑ), Pugh ratio, and Cauchy's pressure are computed as $E = \frac{9KG}{3K+G}$, $\vartheta = \frac{3K - 2G}{2(3K+G)}$, Pughratio=$\frac{G}{K}$, and *Cauchy's Pressure* = C_{12}−C_{44}. Finally, hardness (H) is determined as $H_1 = 0.1769G - 2.899$[64] and $H_2 = 0.0635E$; $H = (H_1 + H_2)/2$.[65]

We use MechElastic[66] and ELATE[67] code to postprocess the elastic tensors. We used the same DFT model to calculate the mechanical properties of experimentally reported borides. Differential charge densities are illustrated using Vesta.[68]

■ ASSOCIATED CONTENT

Data Availability Statement

The authors will make available, upon request, the data used in the applications described in this work. It is understood that the data provided will not be for commercial use.

Supporting Information

Properties and phase characteristics of multicomponent and constituent element borides. The Supporting Information is available free of charge at https://pubs.acs.org/doi/10.1021/acs.chemmater.3c01086.

Multicomponent borides and constituent element borides (XLSX)

Accession Codes

The authors will make available, upon request, the code used in the applications described in this work. It is understood that the code will not be for commercial use.

■ AUTHOR INFORMATION

Corresponding Author

Ganesh Balasubramanian − *Institute for Functional Materials & Devices, Lehigh University, Bethlehem, Pennsylvania 18015, United States;* Present Address: Address: Packard Lab 561, 19 Memorial Drive W, Bethlehem, PA 18015; orcid.org/0000-0003-1834-5501; Phone: 610-758-3784; Email: bganesh@lehigh.edu

Author

Prince Sharma − *Institute for Functional Materials & Devices, Lehigh University, Bethlehem, Pennsylvania 18015, United States*

Complete contact information is available at: https://pubs.acs.org/10.1021/acs.chemmater.3c01086

Author Contributions

P.S. developed the formalism and did the analysis and is the primary author of this work. G.B. contributed to the discussion of the correlation of structural properties with the boride material features. Both authors cowrote, edited, and revised the manuscript.

Notes

The authors declare no competing financial interest.

■ ACKNOWLEDGMENTS

This work was supported, in part, by National Science Foundation awards # 1944040 and 2019035. We acknowledge the Texas Advanced Computing Center (TACC) at The University of Texas at Austin for providing Frontera resources that have contributed to the research results reported here. P.S. thanks the support of the P3 program and the University Fellowship at Lehigh.

■ REFERENCES

(1) Samsonov, G. V.; Pryadko, I. F.; Pryadko, L. F. Physicochemical Properties of Transition Metals and of Their Alloys and Compounds. *A Configurational Model of Matter*; Springer US, 1973; pp 33−272. DOI: 10.1007/978-1-4684-1608-4_3.

(2) Golla, B. R.; Mukhopadhyay, A.; Basu, B.; Thimmappa, S. K. Review on Ultra-High Temperature Boride Ceramics. *Prog. Mater. Sci.* **2020**, *111*, 100651.

(3) Pangilinan, L. E.; Hu, S.; Hamilton, S. G.; Tolbert, S. H.; Kaner, R. B. Hardening Effects in Superhard Transition-Metal Borides. *Acc. Mater. Res.* **2022**, *3* (1), 100−109.

(4) Castaing, J.; Costa, P. Properties and Uses of Diborides. In *Boron and Refractory Borides*; Samsonov, G. V., Matkovich, V. I., Hagenmuller, P., Lundstrom, T., Eds.; Springer Berlin Heidelberg: Berlin, Heidelberg, 1977; pp 390−412.

(5) Akopov, G.; Yeung, M. T.; Kaner, R. B.; Akopov, G.; Yeung, M. T.; Kaner, R. B. Rediscovering the Crystal Chemistry of Borides. *Adv. Mater.* **2017**, *29* (21), 1604506.

(6) Lundstrom, T. Structure, defects and properties of some refractory borides. *Pure Appl. Chem.* **1985**, *57* (10), 1383−1390.

(7) Matkovich, V. I. Structural Principles in Refractory Borides. *Pure Appl. Chem.* **1974**, *39* (4), 525−545.

(8) Albert, B.; Hofmann, K. Metal Borides: Versatile Structures and Properties. *Handbook of Solid State Chemistry*; John Wiley & Sons, Ltd, 2017, pp 435−453. DOI: 10.1002/9783527691036.HSSCVOL1011.

(9) Scheifers, J. P.; Zhang, Y.; Fokwa, B. P. T. Boron: Enabling Exciting Metal-Rich Structures and Magnetic Properties. *Acc. Chem. Res.* **2017**, *50* (9), 2317−2325.

(10) Jiang, X.; Zhao, J. Evolution of Boron Clusters in Iron Tetraborides under High Pressure: Semiconducting and Ferromagnetic Superhard Materials. *RSC Adv.* **2015**, *5* (59), 48012−48023.
(11) Mukhopadhyay, A.; Golla, B. R.; Basu, B. Ultra High Temperature Ceramics: Processing, Properties, and Applications. In *MAX Phases and Ultra-high Temperature Ceramics for Extreme Environments*; IGI Global, pp 49−99.
(12) Ni, D.; Cheng, Y.; Zhang, J.; Liu, J. X.; Zou, J.; Chen, B.; Wu, H.; Li, H.; Dong, S.; Han, J.; Zhang, X.; Fu, Q.; Zhang, G. J. Advances in Ultra-High Temperature Ceramics, Composites, and Coatings. *J. Adv. Ceram.* **2022**, *11* (1), 1−56.
(13) Iwan, S.; Lin, C. M.; Perreault, C.; Chakrabarty, K.; Chen, C. C.; Vohra, Y.; Hrubiak, R.; Shen, G.; Velisavljevic, N. High-Entropy Borides under Extreme Environment of Pressures and Temperatures. *Materials* **2022**, *15* (9), 3239.
(14) Gild, J.; Zhang, Y.; Harrington, T.; Jiang, S.; Hu, T.; Quinn, M. C.; Mellor, W. M.; Zhou, N.; Vecchio, K.; Luo, J. High-Entropy Metal Diborides: A New Class of High-Entropy Materials and a New Type of Ultrahigh Temperature Ceramics. *Sci. Rep.* **2016**, *6* (1), 37946−38010.
(15) Akrami, S.; Edalati, P.; Fuji, M.; Edalati, K. High-Entropy Ceramics: Review of Principles, Production and Applications. *Mater. Sci. Eng. R Rep.* **2021**, *146*, 100644.
(16) Yeh, J. W.; Chen, S. K.; Lin, S. J.; Gan, J. Y.; Chin, T. S.; Shun, T. T.; Tsau, C. H.; Chang, S. Y. Nanostructured High-Entropy Alloys with Multiple Principal Elements: Novel Alloy Design Concepts and Outcomes. *Adv. Eng. Mater.* **2004**, *6* (5), 299−303.
(17) Cantor, B.; Chang, I. T. H.; Knight, P.; Vincent, A. J. B. Microstructural Development in Equiatomic Multicomponent Alloys. *J. Mater. Sci. Eng. A* **2004**, *375*−*377* (1−2), 213−218.
(18) Akopov, G.; Pangilinan, L. E.; Mohammadi, R.; Kaner, R. B. Perspective: Superhard Metal Borides: A Look Forward. *APL Mater.* **2018**, *6* (7), 070901.
(19) Kavak, S.; Bayrak, K. G.; Mansoor, M.; Kaba, M.; Ayas, E.; Balcı-Çağıran, Ö.; Derin, B.; Öveçoğlu, M. L.; Ağaoğulları, D. First Principles Calculations and Synthesis of Multi-Phase (HfTiWZr) B2 High Entropy Diboride Ceramics: Microstructural, Mechanical and Thermal Characterization. *J. Eur. Ceram. Soc.* **2023**, *43* (3), 768−782.
(20) Murchie, A. C.; Watts, J. L.; Fahrenholtz, W. G.; Hilmas, G. E. Room-Temperature Mechanical Properties of a High-Entropy Diboride. *Int. J. Appl. Ceram. Technol.* **2022**, *19* (4), 2293−2299.
(21) Zhang, Y.; Jiang, Z. B.; Sun, S. K.; Guo, W. M.; Chen, Q. S.; Qiu, J. X.; Plucknett, K.; Lin, H. T. Microstructure and Mechanical Properties of High-Entropy Borides Derived from Boro/Carbothermal Reduction. *J. Eur. Ceram. Soc.* **2019**, *39* (13), 3920−3924.
(22) Liu, J.; Yang, Q. Q.; Zou, J.; Wang, W. M.; Wang, X. G.; Fu, Z. Y. Strong High-Entropy Diboride Ceramics with Oxide Impurities at 1800°C. *Sci. China Mater.* **2023**, *66*, 2061−2070.
(23) Yang, Y.; Bi, J.; Sun, K.; Qiao, L.; Liu, Y.; Li, Y.; Wang, H.; Liang, Y.; Shang, M. Novel (Hf0.2Zr0.2Ta0.2V0.2Nb0.2) B2 High Entropy Diborides with Superb Hardness Sintered by SPS under a Mild Condition. *Ceram. Int.* **2022**, *48* (20), 30859−30867.
(24) Feng, L.; Fahrenholtz, W. G.; Hilmas, G. E. Processing of Dense High-Entropy Boride Ceramics. *J. Eur. Ceram. Soc.* **2020**, *40* (12), 3815−3823.
(25) Storr, B.; Moore, L.; Chakrabarty, K.; Mohammed, Z.; Rangari, V.; Chen, C. C.; Catledge, S. A. Properties of High Entropy Borides Synthesized via Microwave-Induced Plasma. *APL Mater.* **2022**, *10* (6), 061109.
(26) Zhang, Y.; Sun, S. K.; Guo, W. M.; Zhang, W.; Xu, L.; Yuan, J. H.; Guan, D. K.; Wang, D. W.; You, Y.; Lin, H. T. Fabrication of Textured (Hf0.2Zr0.2Ta0.2Cr0.2Ti0.2) B2 High-Entropy Ceramics. *J. Eur. Ceram. Soc.* **2021**, *41* (1), 1015−1019.
(27) Zhang, Y.; Guo, W. M.; Jiang, Z. B.; Zhu, Q. Q.; Sun, S. K.; You, Y.; Plucknett, K.; Lin, H. T. Dense High-Entropy Boride Ceramics with Ultra-High Hardness. *Scr. Mater.* **2019**, *164*, 135−139.
(28) Zou, Q.; Gu, H.; Li, Y.; Li, Z.; Liang, P.; Luo, Y. Characterization and Analysis of High-Entropy Boride Ceramics Sintered at Low Temperature. *J. Am. Ceram. Soc.* **2023**, *106*, 2764−2772.
(29) Qin, M.; Gild, J.; Wang, H.; Harrington, T.; Vecchio, K. S.; Luo, J. Dissolving and Stabilizing Soft WB2 and MoB2 Phases into High-Entropy Borides via Boron-Metals Reactive Sintering to Attain Higher Hardness. *J. Eur. Ceram. Soc.* **2020**, *40* (12), 4348−4353.
(30) Feltrin, A. C.; Hedman, D.; Akhtar, F. Transformation of Metastable Dual-Phase (Ti0.25V0.25Zr0.25Hf0.25) B2 to Stable High-Entropy Single-Phase Boride by Thermal Annealing. *Appl. Phys. Lett.* **2021**, *119* (16), 161905.
(31) Feng, L.; Monteverde, F.; Fahrenholtz, W. G.; Hilmas, G. E. Superhard High-Entropy AlB2-Type Diboride Ceramics. *Scr. Mater.* **2021**, *199*, 113855.
(32) Li, Q.; Zhou, D.; Zheng, W.; Ma, Y.; Chen, C. Global Structural Optimization of Tungsten Borides. *Phys. Rev. Lett.* **2013**, *110* (13), 136403.
(33) Kvashnin, A. G.; Zakaryan, H. A.; Zhao, C.; Duan, Y.; Kvashnina, Y. A.; Xie, C.; Dong, H.; Oganov, A. R. New Tungsten Borides, Their Stability and Outstanding Mechanical Properties. *J. Phys. Chem. Lett.* **2018**, *9* (12), 3470−3477.
(34) Zhao, E.; Meng, J.; Ma, Y.; Wu, Z. Phase Stability and Mechanical Properties of Tungsten Borides from First Principles Calculations. *Phys. Chem. Chem. Phys.* **2010**, *12* (40), 13158−13165.
(35) Yu, R.; Zhang, Q.; Zhan, Q. Softest Elastic Mode Governs Materials Hardness. *Chin. Sci. Bull.* **2014**, *59* (15), 1747−1754.
(36) Pauling, L. *The Nature of the Chemical Bond and the Structure of Molecules and Crystals: An Introduction to Modern Structural Chemistry*; 3rd ed.; Cornell University Press: Ithaca, NY, 1960.
(37) Harrison, W. A. *Electronic Structure and the Properties of Solids: The Physics of the Chemical Bond*; Courier Corporation, 2012.
(38) West, A. R. *Solid State Chemistry and its Applications*, 2nd ed.; John Wiley & Sons, 2022.
(39) Raghavan, V. *Materials Science and Engineering: A First Course*; 6th ed.; PHI Learning Pvt. Ltd., 2015.
(40) Li, W.; Xie, D.; Li, D.; Zhang, Y.; Gao, Y.; Liaw, P. K. Mechanical Behavior of High-Entropy Alloys. *Prog. Mater. Sci.* **2021**, *118*, 100777.
(41) George, E. P.; Curtin, W. A.; Tasan, C. C. High Entropy Alloys: A Focused Review of Mechanical Properties and Deformation Mechanisms. *Acta Mater.* **2020**, *188*, 435−474.
(42) Murty, B. S.; Yeh, J. W.; Ranganathan, S.; Bhattacharjee, P. P. Structural Properties. *High-Entropy Alloys*; Elsevier, 2019; pp 195−232.
(43) Qin, M.; Shivakumar, S.; Lei, T.; Gild, J.; Hessong, E. C.; Wang, H.; Vecchio, K. S.; Rupert, T. J.; Luo, J. Processing-Dependent Stabilization of a Dissimilar Rare-Earth Boride in High-Entropy (Ti0.2Zr0.2Hf0.2Ta0.2Er0.2) B2 with Enhanced Hardness and Grain Boundary Segregation. *J. Eur. Ceram. Soc.* **2022**, *42* (12), 5164−5171.
(44) Qin, M.; Gild, J.; Hu, C.; Wang, H.; Hoque, M. S. B.; Braun, J. L.; Harrington, T. J.; Hopkins, P. E.; Vecchio, K. S.; Luo, J. Dual-Phase High-Entropy Ultra-High Temperature Ceramics. *J. Eur. Ceram. Soc.* **2020**, *40* (15), 5037−5050.
(45) Feng, L.; Fahrenholtz, W. G.; Hilmas, G. E.; Monteverde, F. Effect of Nb Content on the Phase Composition, Densification, Microstructure, and Mechanical Properties of High-Entropy Boride Ceramics. *J. Eur. Ceram. Soc.* **2021**, *41* (1), 92−100.
(46) Zhang, Y.; Sun, S. K.; Zhang, W.; You, Y.; Guo, W. M.; Chen, Z. W.; Yuan, J. H.; Lin, H. T. Improved Densification and Hardness of High-Entropy Diboride Ceramics from Fine Powders Synthesized via Borothermal Reduction Process. *Ceram. Int.* **2020**, *46* (9), 14299−14303.
(47) Wang, Y. P.; Gan, G. Y.; Wang, W.; Yang, Y.; Tang, B. Y. Ab Initio Prediction of Mechanical and Electronic Properties of Ultrahigh Temperature High-Entropy Ceramics (Hf0.2Zr0.2Ta0.2M0.2Ti0.2) B2 (M = Nb, Mo, Cr). *Phys. Status Solidi B* **2018**, *255* (8), 1800011.
(48) Qiao, L.; Liu, Y.; Gao, Y.; Bi, J.; Li, Y.; Liu, C.; Gao, J.; Wang, W.; Qian, Z. First-Principles Prediction, Fabrication and Characterization of (Hf0.2Nb0.2Ta0.2Ti0.2Zr0.2) B2 High-Entropy Borides. *Ceram. Int.* **2022**, *48* (12), 17234−17245.

https://doi.org/10.1021/acs.chemmater.3c01086
Chem. Mater. 2023, 35, 7511−7520

(49) Yao, G.; Wang, W. Y.; Li, P. X.; Ren, K.; Lu, J. Q.; Gao, X. Y.; Lin, D. Y.; Wang, J.; Wang, Y. G.; Song, H. F.; Liu, Z. K.; Li, J. S. Electronic Structures and Strengthening Mechanisms of Superhard High-Entropy Diborides. *Rare Met.* **2023**, *42* (2), 614−628.
(50) Wang, H. Y.; Xue, F. Y.; Zhao, H.; Li, D. J. First-Principles Calculation of Elastic Properties of TiB_2 and ZrB_2. *Adv. Mater. Res.* **2010**, *150*−*151*, 40−43.
(51) Ledbetter, H.; Tanaka, T. Elastic-Stiffness Coefficients of Titanium Diboride. *J. Res. Natl. Inst. Stand. Technol.* **2009**, *114* (6), 333.
(52) Dai, F. Z.; Sun, Y.; Wen, B.; Xiang, H.; Zhou, Y. Temperature Dependent Thermal and Elastic Properties of High Entropy (Ti0.2Zr0.2Hf0.2Nb0.2Ta0.2) B2: Molecular Dynamics Simulation by Deep Learning Potential. *J. Mater. Sci. Technol.* **2021**, *72*, 8−15.
(53) Sharma, P.; Balasubramanian, G. High Configurational Entropy Driven Increased Heat Capacity of Refractory Multicomponent Di-Silicides. *Materialia* **2023**, *30*, 101861.
(54) Tao, Q.; Zheng, D.; Zhao, X.; Chen, Y.; Li, Q.; Li, Q.; Wang, C.; Cui, T.; Ma, Y.; Wang, X.; Zhu, P. Exploring Hardness and the Distorted Sp2 Hybridization of B-B Bonds in WB3. *Chem. Mater.* **2014**, *26* (18), 5297−5302.
(55) Samsonov, G. V.; Serebryakova, T. I. Classification of Borides. *Sov. Powder Metall. Met. Ceram.* **1978**, *17* (2), 116−120.
(56) Kresse, G.; Furthmüller, J. Efficient Iterative Schemes for *Ab Initio* Total-Energy Calculations Using a Plane-Wave Basis Set. *Phys. Rev. B* **1996**, *54* (16), 11169−11186.
(57) Wang, V.; Xu, N.; Liu, J. C.; Tang, G.; Geng, W. T. VASPKIT: A User-Friendly Interface Facilitating High-Throughput Computing and Analysis Using VASP Code. *Comput. Phys. Commun.* **2021**, *267*, 108033.
(58) van de Walle, A.; Asta, M.; Ceder, G. The Alloy Theoretic Automated Toolkit: A User Guide. *Calphad* **2002**, *26* (4), 539−553.
(59) Kresse, G.; Joubert, D. From Ultrasoft Pseudopotentials to the Projector Augmented-Wave Method. *Phys. Rev. B* **1999**, *59* (3), 1758−1775.
(60) Perdew, J. P.; Burke, K.; Ernzerhof, M. Generalized Gradient Approximation Made Simple. *Phys. Rev. Lett.* **1996**, *77* (18), 3865−3868.
(61) Payne, M. C.; Teter, M. P.; Allan, D. C.; Arias, T. A.; Joannopoulos, J. D. Iterative Minimization Techniques for *Ab Initio* Total-Energy Calculations: Molecular Dynamics and Conjugate Gradients. *Rev. Mod. Phys.* **1992**, *64* (4), 1045−1097.
(62) Monkhorst, H. J.; Pack, J. D. Special Points for Brillouin-Zone Integrations. *Phys. Rev. B* **1976**, *13* (12), 5188−5192.
(63) Nye, J. F. *Physical Properties of Crystals Representation by Tensors and Matrices*; Clarendon Press, 1985.
(64) Teter, D. M. Computational Alchemy: The Search for New Superhard Materials. *MRS Bull.* **1998**, *23* (1), 22−27.
(65) Jiang, X.; Zhao, J.; Wu, A.; Bai, Y.; Jiang, X. Mechanical and electronic properties of B_{12}-based ternary crystals of orthorhombic phase. *J. Phys.: Condens. Matter* **2010**, *22* (31), 315503.
(66) Singh, S.; Lang, L.; Dovale-Farelo, V.; Herath, U.; Tavadze, P.; Coudert, F. X.; Romero, A. H. MechElastic: A Python Library for Analysis of Mechanical and Elastic Properties of Bulk and 2D Materials. *Comput. Phys. Commun.* **2021**, *267*, 108068.
(67) Gaillac, R.; Pullumbi, P.; Coudert, F. X. ELATE: An Open-Source Online Application for Analysis and Visualization of Elastic Tensors. *J. Phys.: Condens. Matter* **2016**, *28* (27), 275201.
(68) Momma, K.; Izumi, F. VESTA: A Three-Dimensional Visualization System for Electronic and Structural Analysis. *J. Appl. Crystallogr.* **2008**, *41* (3), 653−658.

https://doi.org/10.1021/acs.chemmater.3c01086
Chem. Mater. 2023, 35, 7511−7520